

18 **Abstract**

19 We present the first water vapor profiles encompassing the upper mesosphere of Mars, 100–120
20 km, far exceeding the maximum altitudes where remote sensing has been able to observe water
21 to date. Our results are based on solar occultation measurements by Atmospheric Chemistry
22 Suite (ACS) onboard the ExoMars Trace Gas Orbiter (TGO). The observed wavelength range
23 around 2.7 μm possesses strong CO_2 and H_2O absorption lines allowing sensitive temperature
24 and density retrievals. We report a maximum H_2O mixing ratio varying from 10 to 50 ppmv at
25 100–120 km during the global dust storm (GDS) of Martian Year (MY) 34 and around southern
26 summer solstice of MY 34 and 35. During other seasons water remains persistently below ~ 2
27 ppmv. We claim that contributions of the MY34 GDS and perihelion periods into the projected
28 hydrogen escape from Mars are nearly equivalent.

29 **Plain Language Summary**

30 We report regular events of high abundances of the water vapor (H_2O) in the upper atmosphere
31 of Mars (100–120 km). So far, any water enrichment has not been revealed by remote sensing at
32 such high altitudes. Higher than 80 km, solar light breaks water vapor molecules into H and O
33 atoms, which may reach the exosphere and escape the planet. When Mars is closer to the Sun
34 (the perihelion season), the atmosphere's circulation intensifies, causing increased dust activity
35 with global dust storms (GDS), occurring every 3–4 Mars years. We observed during the second
36 halves of Martian years 34 and 35 (2018–2020), including one GDS and two perihelion seasons.
37 We report that the maximum water relative abundance reaches 10–50 parts per million in volume
38 (ppmv) at 100–120 km during the GDS and every perihelion season. These high values indicate
39 that the Martian atmosphere above 100 km regularly hosts large amounts of water, facilitating
40 the long-term escape of water from the planet.

41 **1 Introduction**

42 The vertical distribution of water vapor (H_2O) on Mars is an indicator of the intricate
43 coupling of distinct phenomena: temperature variations, cloud formation, sublimation, turbulent
44 and convective mixing, as well as general circulation and wave/eddy transport. H_2O has long
45 been thought to remain confined below the hygropause, which is the level where the saturation
46 condition is met and where water ice clouds may form, as occurs on Earth. The existence of this
47 layer on Mars was established for the first time by ground-based microwave soundings of Clancy
48 et al. (1996) with a saturation level between 10–20 km around the aphelion, i.e., Solar
49 Longitudes (L_S) 70° , and 40–60 km around perihelion (L_S 250°). In parallel, Rodin et al. (1997)
50 reported water vapor profiles retrieved from the solar occultations made by Auguste on Phobos-2
51 in 1989. The existence of a hygropause at 30–35 km (with a mixing ratio of 3 ppm) in the
52 northern spring ($L_S=0^\circ$ – 20°) near the equator was subsequently claimed. The first climatology of
53 water vapor profiles was derived from SPICAM-IR solar occultations on Mars Express (MEx)
54 (Fedorova et al., 2009; 2018; 2021; Maltagliati et al., 2013), covering eight Martian years. The
55 hygropause level was found to vary from 40 to 80 km depending on season, latitude, and dust
56 events. Hygropause is also indirectly sensed in CRISM limb profiles of $\text{O}_2(^1\Delta\text{g})$ emission, a
57 confident indicator of O_3 , from which water vapor mixing ratios were inferred by Clancy et al.
58 (2017).

59 The observation of large amounts of water vapor in and above the middle atmosphere
60 (>40 km, Maltagliati et al., 2013) was then complemented by the discovery of short-term decline

61 of the hydrogen corona brightness over several weeks (Chaffin et al., 2014; Clarke et al., 2014).
62 This variability exposed a new paradigm in our perception of how water escapes from Mars
63 (Chaffin et al., 2017). So far, water escape was thought to be controlled by a slow conversion
64 process involving H_2 , formed from the catalytic recombination of carbon dioxide with odd
65 hydrogen (McElroy and Donahue, 1972; Krasnopolsky, 2002). The non-condensable H_2 can
66 overcome the hygropause and reach the mesosphere (80–120 km), while transported by turbulent
67 mixing or circulation. There, it can dissociate and release H atoms that will escape the planet
68 once above the exobase.

69 Observations have revealed that water vapor transport from the troposphere to the lower
70 mesosphere of Mars occurs during the dusty season and is enhanced at times of major dust
71 storms. In particular, a significant H_2O enhancement in the middle atmosphere was observed
72 during the global dust storm (GDS) in 2007 (MY28) with a rise of the hygropause altitude to >60
73 km (Fedorova et al., 2018; Heavens et al., 2018; 2019). Sensitive solar occultation measurements
74 by NOMAD and ACS NIR instruments onboard the ExoMars Trace Gas Orbiter (TGO) have
75 showed that water vapor reached 80–100 km (Aoki et al., 2019; Fedorova et al., 2020) during
76 two storms in 2018 and 2019 (a global one at L_S 190°–220° and a regional one at L_S 330° in
77 MY34; Montabone et al., 2020). Fedorova et al. (2020) revealed the water supersaturation at 70–
78 90 km even in the presence of H_2O ice clouds not only during the GDS but also near the
79 Southern summer solstice ($L_S \sim 270^\circ$) when water reached 90–100 km as well. Altogether, these
80 studies promote a new mechanism for controlling H escape through direct delivery at above 80
81 km and further photodissociation of H_2O molecules (Chaffin et al., 2017; Krasnopolsky et al.,
82 2019). General circulation models predict an upward water flux into the thermosphere (>120 km)
83 during the GDS and perihelion periods (Shaposhnikov et al., 2019; Neary et al., 2020; Rossi et
84 al. 2021).

85 The discussion regarding a relative contribution of perihelion or GDS to the mesospheric
86 water enrichment was recently stimulated by SPICAM/MEEx long-term observations covering
87 Martian Years 28 through 35. Here, Fedorova et al. (2021) claimed an annual rise of water
88 abundance up to ~90 km in perihelion, which is compatible with GDS enhancements. The new
89 ACS/TGO dataset confirms those conclusions for altitudes below 100 km in MY34–MY35
90 (Fedorova et al. 2020, Alday et al., 2021). In parallel, during the perihelion season, the D/H ratio
91 in water decreases with altitude from 4–6 times SMOW (Standard Mean Ocean Water) in the
92 lower atmosphere to 2–3 times in the mesosphere (50–70 km) as measured by ACS MIR (Alday
93 et al., 2021) and NOMAD (Villanueva et al., 2021) spectrometers. Alday et al. (2021) show that
94 ultraviolet H_2O photolysis dominates the production of H relative to D atoms in the upper
95 atmosphere.

96 From above, ion chemistry in the thermosphere has been characterized by the NGIMS
97 mass-spectrometer on MAVEN (Benna et al., 2015) and interpreted by the ionospheric model of
98 Fox et al. (2015). Using NGIMS data, Stone et al. (2020) measured H_2O ion concentrations
99 around ~150 km for the 2014–2018 period (MY32–MY34). With the help of the model by Fox et
100 al. (2015), Stone et al. (2020) found the relative abundance of water at this altitude on the
101 dayside varying seasonally on average from 2 to 5 ppm. Several enhanced dusty episodes disrupt
102 this seasonal signal: 3–9 ppm during the regional storm of MY32, 10–20 ppm during the storm
103 of MY33, and up to 60 ppm in the GDS of MY34. Stone et al. (2020) concluded that water
104 transport into the ionosphere and its destruction are the main mechanisms in the overall hydrogen
105 escape from Mars.

106 We used the data of the middle infrared spectrometer of the Atmospheric Chemistry Suite
107 (ACS MIR) onboard the ExoMars TGO, which measures water vapor VMR and atmospheric
108 density in a wide range of altitudes, from the troposphere to the lower thermosphere, using the
109 strong absorption bands of H₂O and CO₂ around 2.66–2.70 μm. The high spectral resolution and
110 the good signal-to-noise ratio of ACS MIR allow the measurements of water profiles up to 120
111 km, inaccessible altitudes for the ACS NIR and SPICAM measurements, sensing the 1.38 μm
112 absorption band (Fedorova et al., 2020; 2021). The strong H₂O absorption around 2.6 μm is also
113 used by NOMAD, yielding water profiles up to ~90 km (Aoki et al., 2019; Villanueva et al.,
114 2021).

115 Here we report the first water vapor abundance measurements in the upper mesosphere
116 (up to 120 km) of Mars. The goal of our paper is to compare the mesospheric water behavior
117 between the second halves of MY34 and MY35 when the high H₂O content is observed. We aim
118 to clarify the principal mechanism of H₂O delivery to the upper mesosphere: it is sporadic dust
119 events, or the result of seasonal variability in the Martian circulation that peaks each year, around
120 Southern summer solstice. For that, we analyze seasonal and latitudinal variations of H₂O VMR
121 vertical profiles retrieved from the ACS MIR solar occultation experiment.

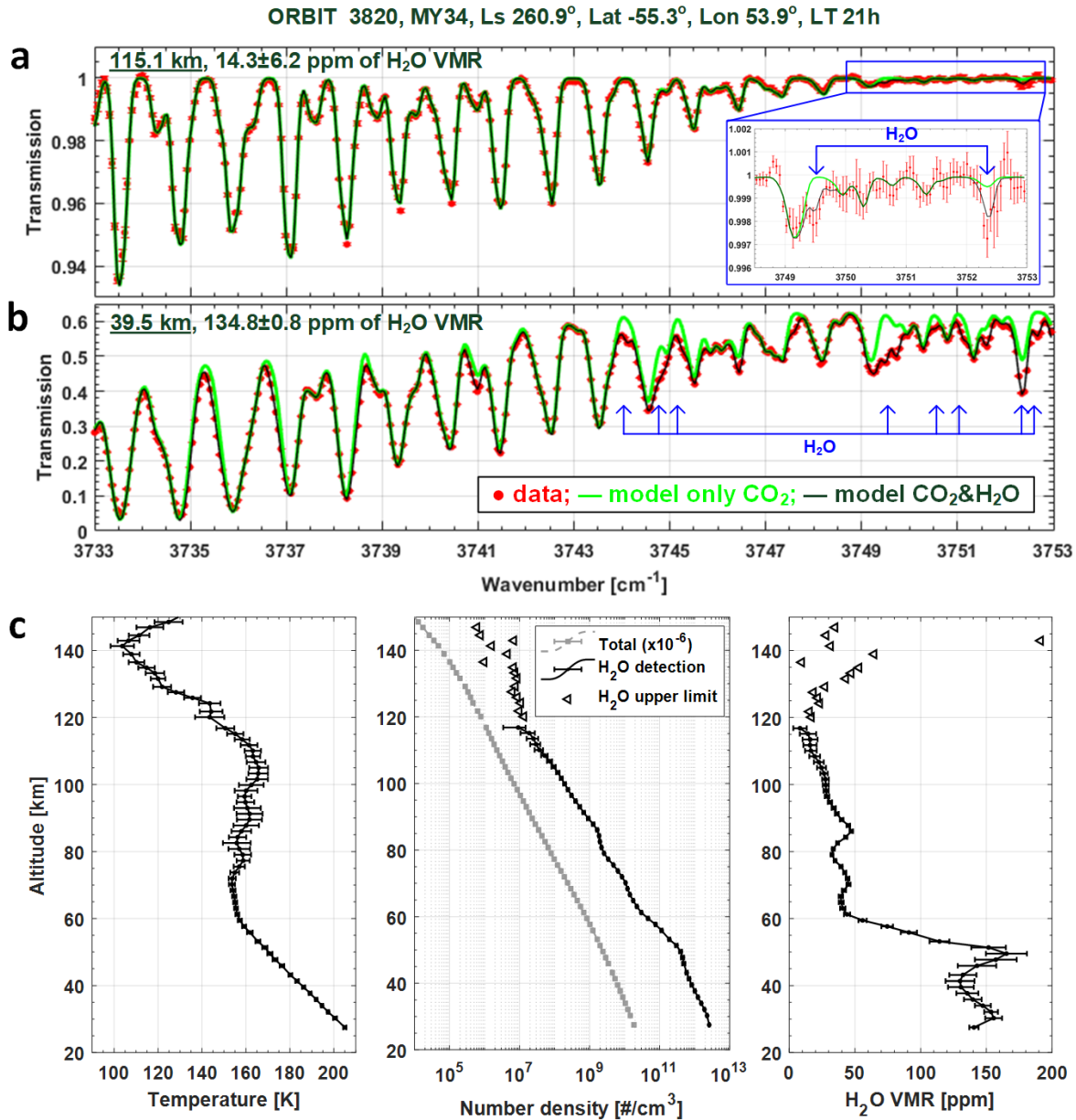
122 **2 Measurements and dataset overview**

123 **2.1 ACS MIR spectroscopy and retrievals**

124 ACS MIR, a solar occultation cross-dispersion echelle spectrometer, records spectra from
125 a set of adjacent diffraction orders (from 10 to 20 per occultation) projected onto a 2D detector
126 array (Korablev et al., 2018). To retrieve high altitude water vapor abundances together with the
127 atmospheric temperature and pressure, we use MIR spectra from the diffraction order #223. They
128 cover a narrow wavelength interval of 2.66–2.68 μm (3733–3753 cm⁻¹), including a part of the
129 2.7-μm CO₂ absorption band and a few strong H₂O lines near 2.66 μm (Fig. 1a, 1b, Fig. S1). The
130 instrument's spectral resolution is ~0.15 cm⁻¹, while the signal-to-noise ratio ranges from 2,000
131 to 4,000, which provides high sensitivity for detections in the upper atmosphere where
132 atmospheric constituent densities are low. Temperature (Fig. 1c) is retrieved by fitting a
133 synthetic model to the CO₂ rotational band taking advantage of its temperature dependence as
134 seen in Fig. S1 of the Supplementary Material (SM). This procedure was applied iteratively, with
135 the pressure calculated from the retrieved temperature profile under the assumption of
136 hydrostatic equilibrium. The temperature measurements were then validated against those made
137 by MIR near the 2.6 μm CO₂ band (Alday et al., 2019) and by ACS NIR around the 1.58 μm
138 band (Fedorova et al., 2020). As a result, one occultation session allows us to simultaneously
139 retrieve profiles of pressure and temperature (from CO₂ absorption bands) and the H₂O number
140 density (Fig. 2c). The water abundance can then be expressed relative to the total atmospheric
141 density, that is, in VMR (in ppmv). Specific details of the algorithms pertaining to this work can
142 be found in SM.

143 The dataset analyzed here consists of a series of transmission spectra obtained during a
144 solar occultation while the line of sight of the instrument progressively penetrates from the upper
145 into deeper layers of the atmosphere, or vice versa (see examples in Fig. 1a, 1b). The
146 transmission is determined as the solar spectrum ratio measured through the atmosphere to the
147 reference one, taken from the data above a tangent height of 200 km. This altitude level is
148 negligibly attenuated by the atmosphere even within the very strong CO₂ band system at 2.7 μm.

149 The typical integration time is 2 seconds, which provides an altitude resolution ranging from 0.5
 150 to 2.5 km, depending on the occultation duration. It gives sufficiently fine vertical sampling for
 151 an atmosphere whose scale height ranges from 5 to 10 km depending on temperature. The
 152 instrument field of view projected at the limb is around 1-3 km in altitude equivalent.



153

154 **Figure 1.** Example ACS MIR spectra and profiles of the retrieved quantities. Measured
 155 transmission spectra (red) at tangent altitudes of 115.1 km (**a**) and 39.5 km (**b**) are compared
 156 with the best-fit models, including both CO₂ and H₂O absorptions (black), and only CO₂
 157 absorption (green). Blue arrows indicate water absorption lines. Zoom in (**a**) shows a part with
 158 the strongest H₂O absorption detected at 115 km. (**c**) Retrieved vertical profiles of temperature
 159 (left), number densities (center), and H₂O volume mixing ratio (VMR) (right). The atmospheric

160 density (grey squares) is scaled by the factor of 10^{-6} . Black triangles mark H₂O upper limits (see
161 SM for the description of uncertainties).

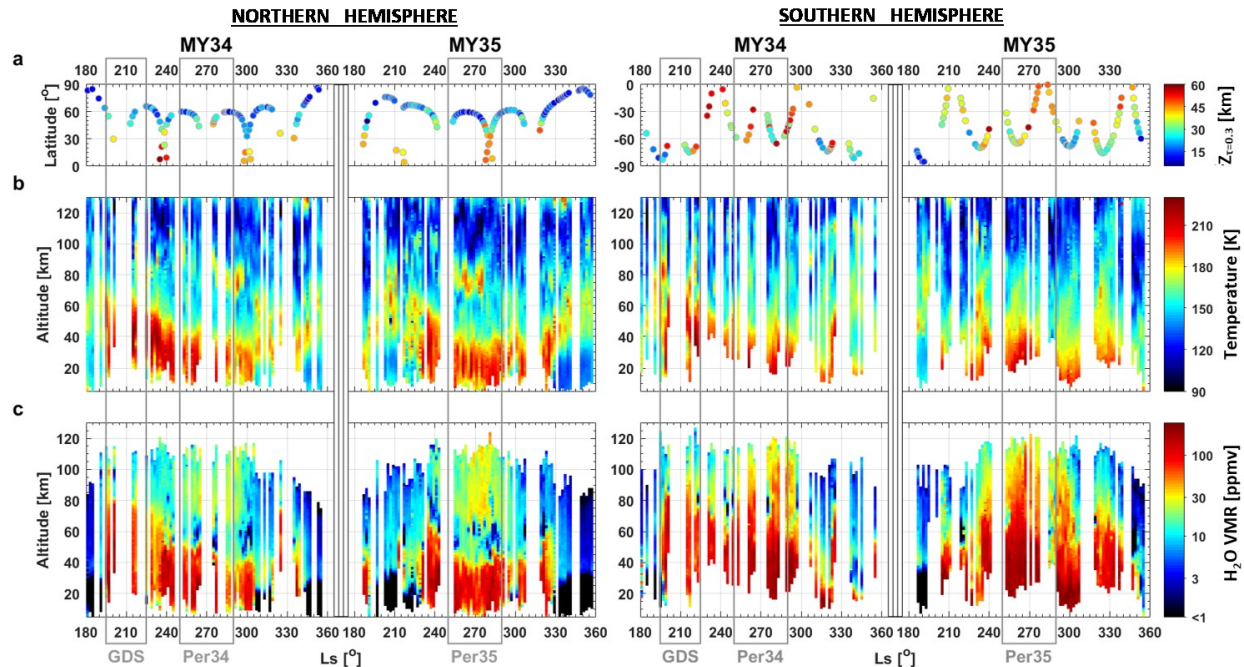
162 2.2 Data selection

163 Our measurements of the mesospheric water focus on the second halves of MY34 and
164 MY35, which correspond to ACS MIR observations from May 2018 to March 2019 and from
165 April 2020 to January 2021. The selected dataset comprises 187 occultation sessions in the
166 Northern Hemisphere and 156 sessions in the Southern Hemisphere, encompassing seasonal
167 periods from L_S 180° to 355° in MY34 and from L_S 185° to 356° in MY35 (Fig. 2a). Figure 2a
168 shows the latitude coverage with the corresponding aerosol activity, which was defined for each
169 occultation at the altitude level where the slant opacity equals 0.3 (~0.75 of the atmospheric
170 transmittance in the continuum). Measurements in the Northern Hemisphere occurred mostly in
171 the high latitude range, between 40°N and 70°N. In the South, the perihelion observations (L_S
172 270°) were made in mid-latitudes, while the rest of occultations occurred close to the polar
173 region (60°S–90°S). Only a few sessions were localized nearby the equator: at L_S~240° and
174 L_S~300° of MY34 and at L_S~210° and L_S~280° of MY35. These observations are accompanied
175 by a higher aerosol loading than for high latitude and polar regions (Fig. 2a).

176 3 Seasonal variation of altitude profiles

177 Observations in the second halves of MY34 and MY35 uncover events, which drastically
178 perturbed the temperature and water vapor vertical distributions. The peculiar pattern to compare
179 with is the MY34 GDS and perihelion periods in MY34 versus MY35, which had no GDS but a
180 regional dust activity in its second half. The seasonal variation of the processed altitude profiles
181 is presented in Figure 2(b, c). We binned the profiles into intervals of 2° in solar longitude and 2
182 km in altitude. Depending on the L_S and altitude sampling, the value in each bin is calculated as
183 the weighted mean of one to five individual points. We excluded all points with 1-sigma
184 uncertainties exceeding 20 K in temperature and 100% of the H₂O mixing ratio. The second
185 rejection criterion corresponds to the detection limit (~10⁷ cm⁻³) of water number density (see in
186 Fig. 1c) that defines the seasonal variations of the uppermost detectable points in Figure 2c.

187 We observe seasonal temperature (Fig. 2b) and H₂O (Fig. 2c) peaks in the middle
188 atmosphere (40–80 km) during the GDS of MY34, L_S 190°–220°, and an additional smaller peak
189 at L_S 320°–330°, corresponding to a regional storm. Moreover, the rise of water vapor to higher
190 altitudes, up to the mesopause at 110–130 km where temperature encounters a minimum, is
191 observed during the two perihelion intervals (L_S 250°–290°) of MY34 and MY35. Here, the
192 Southern summer (Fig. 2c, right panel) is accompanied by a more humid mesosphere (40–60
193 ppm of H₂O) than the Northern Winter (Fig. 2c, left panel) where the mean mesospheric water
194 reaches 20–30 ppmv on average between 80 and 120 km. In contrast, out of the perihelion peak
195 or dust events, i.e. for the selected data at the beginning of the MY34 GDS and at the very end of
196 MY 34, 35, water content above 80 km never exceeds 2-3 ppmv.



197

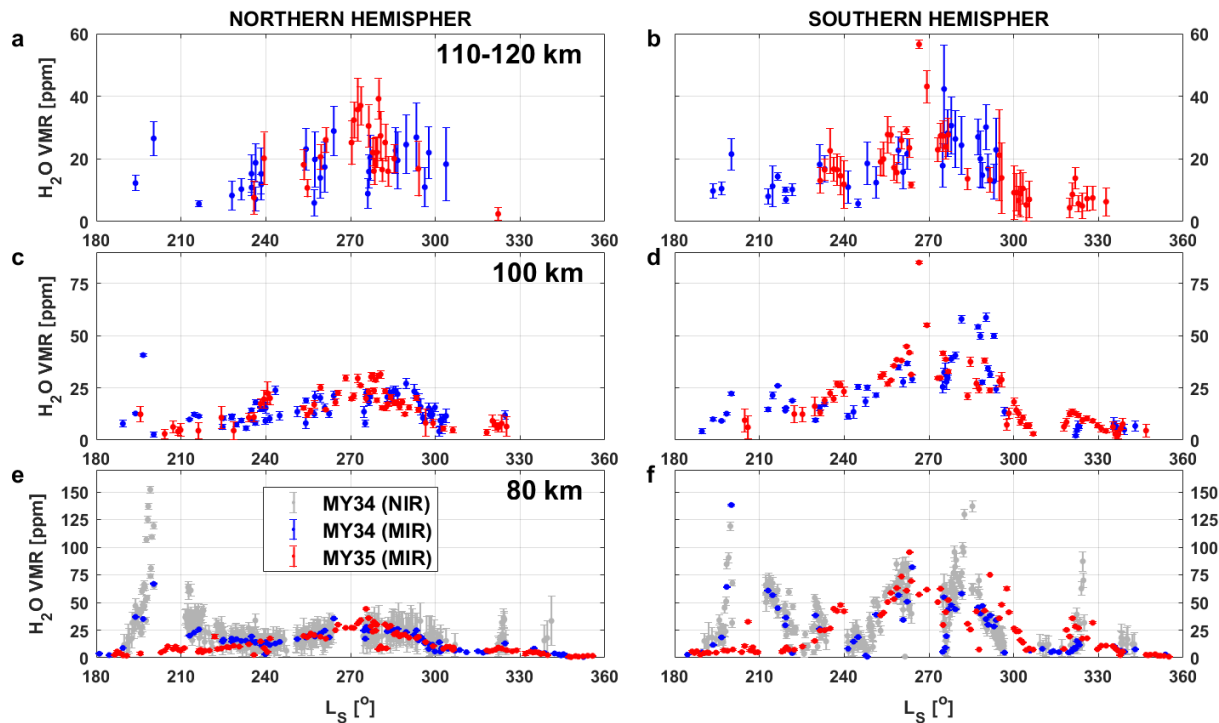
198 **Figure 2.** Seasonal map of atmospheric temperature and H₂O mixing ratio during the second half
 199 of MY34 and MY35. The data are plotted in function of L_S and altitude for the Northern (left)
 200 and the Southern (right) hemispheres. (a) Latitudinal distribution of the ACS-MIR solar
 201 occultations, depending on an altitude level where the aerosol slant opacity (τ) equals 0.3. (b)
 202 Temperature. (c) Volume mixing ratio (VMR) of water vapor. Grey frames outline time intervals
 203 of the global dust storm (GDS) in MY34 and the two perihelions in MY34 (Per34) and MY35
 204 (Per35).

205 4 H₂O variations around perihelion

206 To quantify seasonal trends of water content in the mesosphere, we selected three altitude
 207 layers corresponding to 80 km, 100 km, and 110–120 km. The first layer, which corresponds to
 208 the middle mesosphere, is accessible in all profiles (Fig. 2c) when the vapor concentration
 209 exceeds the detection limit of $\sim 10^7 \text{ cm}^{-3}$, even in low water loading periods. Water at 100–120
 210 km shows up only in stormy periods and around perihelion (Fig. 2c).

211 Observed variations during perihelion for the three selected levels are presented in Figure
 212 3 for both Martian Years. The number of MIR observations at the considered spectral range is
 213 low during the dust storm activity of MY34. Nevertheless, a comparison with MY35 reveals
 214 significant increases of H₂O mixing ratios during the GDS: by a factor of 6–8 at 80 km (Fig. 3e,
 215 3f) and by a factor of 3–5 at 100–120 km from L_S 190° to 220° (Fig. 3a–3d). Increases at L_S
 216 320°–330° follow annually repeatable dust storm activity at this season, although injecting far
 217 less water into the mesosphere than the GDS in MY34. Around Mars perihelion (L_S=240°–300°)
 218 water behaves almost identically between MY34 and MY35. For both Martian Years, the
 219 maximum H₂O mixing ratio was observed near the Southern summer solstice (L_S~270°),
 220 reaching values of 40–80 ppm at 80 km, 30–60 ppm at 100 km, and 20–50 ppm at 110–120 km.
 221 In the Northern winter solstice, it varied from 20 to 40 ppm at all levels, 80–120 km. There are
 222 groups of points out of general behaviour, i.e. at L_S=270°–280° in Fig. 3, that results from
 223 latitudinal variations of the water content (see Fig. S3 in SM). We compare our results at 80 km

224 with the corresponding ACS NIR dataset derived from the MY34 profiles of Fedorova et al.
 225 (2020, grey points in Fig. 3e, 3f). The NIR dataset is five times denser than used in the present
 226 work, and it observed the H₂O seasonal variations in greater detail, especially during the dust
 227 events of MY34.



228
 229 **Figure 3.** Seasonal trends of H₂O volume mixing ratio (VMR) at three altitude levels: 80, 100,
 230 110-120 km. The season is the second halves of MY34 (in blue) and of MY35 (in red). Each
 231 point corresponds to an individual vertical profile: weighted mean value obtained in between
 232 110-120 km (a, b), and interpolated value for the levels of 100 km (c, d) and 80 km (e, f). Data at
 233 80 km in grey (e, f) are taken from the ACS NIR profiles (Fedorova et al., 2020).

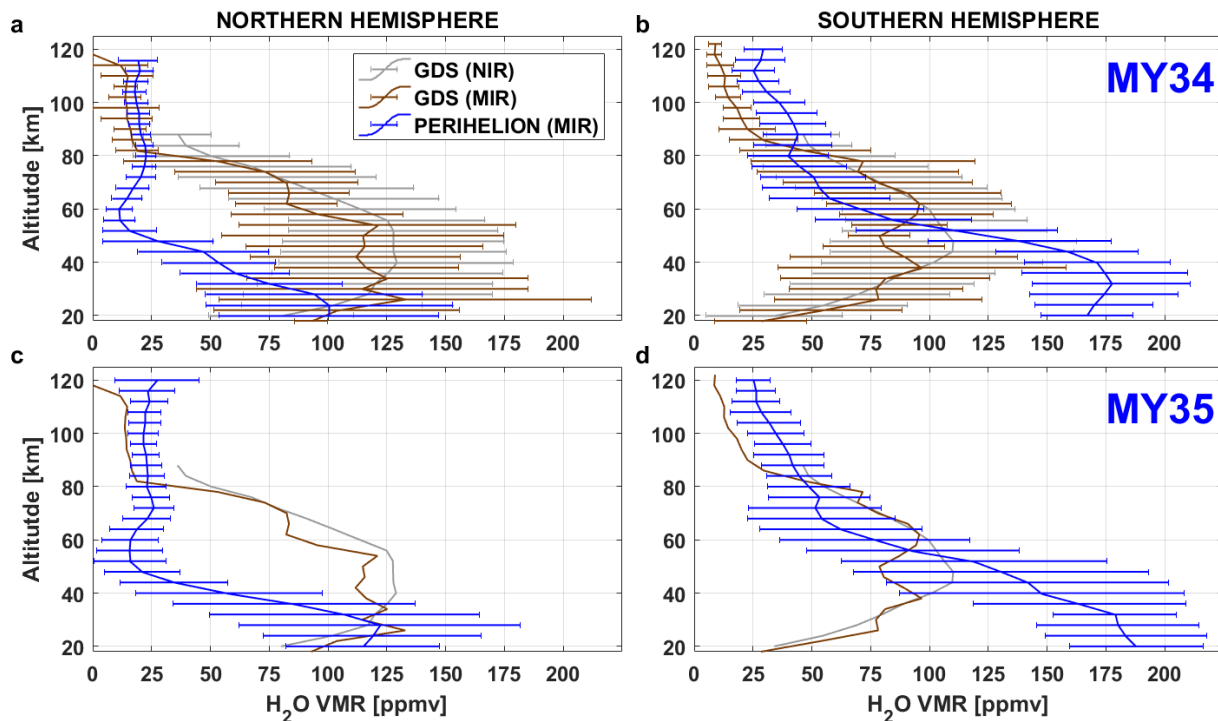
234 4 Discussion and Conclusions

235 For the first time, we report observations of H₂O abundances in a previously unexplored
 236 altitude range (from 100 to 120 km). There we find 10–30 ppm of water vapor during the MY34
 237 GDS and 20–50 ppm around Mars perihelions ($L_s=250^\circ$ – 290°) of MY34 and MY35 in both
 238 hemispheres. Our GDS retrievals at 100–120 km are of the same order of magnitude as MAVEN
 239 NGIMS results reported by Stone et al. (2020) at ~150 km. Surprisingly, NGIMS water
 240 abundances reveal a 2014-2018 mission-wise maximum of H₂O at 150 km, only during the
 241 MY34 GDS, whereas we repeatedly observe the annual maximum around the Southern summer
 242 solstice both in MY34 and MY35.

243 NGIMS measures [H₂O⁺] ions, from which neutral H₂O abundances at 150 km were
 244 derived on the basis of 1D photochemical modeling. The model was adjusted to reproduce the
 245 H₂O VMR at 150 km inferred from the [H₂O⁺] ions measured under two scenarios: low water,
 246 corresponding to 2 ppm prescribed at 80 km in a non-GDS case; and high water of 40 ppm in a
 247 GDS case (Stone et al., 2020; as corrected in March 2021). Notably, all the solar occultation
 248 observations performed by TGO and MEX to date (Fedorova et al., 2018, 2020, 2021; Aoki et

249 al., 2019; Villanueva et al., 2021), including the present dataset (Fig. 3e, 3f), report even higher
 250 water vapor VMRs at 80 km, of 50–80 ppm during the GDS. Stone et al. (2020) indicate a
 251 systematic uncertainty of 69% on their neutral H₂O inference, which is consistent with observed
 252 MAVEN, TGO, and MEX values within such error bars.

253 It is important to consider how ACS's high altitude water vapor abundances combine
 254 with photolysis since this process has been hypothesized to be essential, if not the dominant,
 255 source for the H atoms observed in the exosphere (Chaffin et al., 2017). The conclusion of Stone
 256 et al. (2020) argues for the GDS's predominance and related ion chemistry in the H atoms'
 257 production. Our observations suggest that while the GDS period corresponds to the maximum of
 258 water abundance at 80 km, H₂O at 120 km peaks only later, at the Southern summer solstice,
 259 when it is twice as large as during the GDS. This enhanced solstice maximum suggests that
 260 relative water abundance declines more rapidly above 80 km during the GDS than after, during
 261 perihelion (Fig. 4).



262

263 **Figure 4.** Altitude profiles of average H₂O volume mixing ratio (VMR) during the GDS (MY
 264 34) and the perihelion season (MY 34, 35). The dataset used includes all ACS MIR observations
 265 highlighted in Fig. 2: GDS of MY34 ($L_S=195^\circ-220^\circ$) (brown); the bin around the perihelion
 266 point ($L_S=250^\circ-295^\circ$) (blue). Panels (a, b) for MY34 and (c, d) for MY35 from the Northern (a,
 267 c) and Southern (b, d) hemispheres. Profiles are presented with 1-sigma dispersion over 4-km
 268 altitude bins. Light grey curves are the averages of the NIR data during GDS of MY34
 269 (Fedorova et al., 2020). The GDS curves are also indicated for MY35 to facilitate comparison.
 270 For the data points used in the averaging see Fig. S4 of SM.

271 In Figure 4, we combined altitude profiles from GDS-only ($L_S 195^\circ-220^\circ$) and perihelion
 272 ($L_S 250^\circ-295^\circ$) intervals to compare averaged vertical trends between them. Here, we also see a
 273 coincidence between MIR and NIR GDS profiles in frames of dispersions, which reflect high
 274 variability of the observed GDS points (Fig. S4 of SM). The considered H₂O distributions allow

275 estimating an integral escape flux of the atomic hydrogen in each case. For that, we applied the
276 model of Chaffin et al. (2017), which predicts the atmospheric escape rate depending on the
277 water injection into different altitudes (see Figure 3 of their paper). Our rough calculations show
278 that the H escape flux is about $\sim 5 \times 10^9 \text{ cm}^{-1} \text{ s}^{-1}$ during the considered intervals of MY34's GDS
279 and Southern summer solstices of MY 34 and 35. Thus, we claim nearly equivalent contributions
280 from a single GDS and the perihelion period into the hydrogen escape by the high water
281 enrichment in the middle/upper atmosphere. Fedorova et al. (2021) come to a similar conclusion
282 based on SPICAM/MEx water profiles up to 80 km. A GDS occurs every 3–4 martian years on
283 average (Zurek and Martin, 1993; Wang and Richardson, 2015), making the yearly perihelion
284 contribution to the hydrogen escape reasonable. The water enhancements are tied to the
285 circulation regime (Clancy et al., 1996; Richardson and Wilson, 2002; Montmessin et al., 2005).
286 More measurements and modeling would be needed to decide whether the southern summer
287 solstitial transport, currently near perihelion, or the GDS equinoctial circulation prevailed during
288 the history of Mars.

289 Overall, our results cannot be easily reconciled with water values (up to 60 ppm at 150
290 km) inferred from NGIMS ion measurements, which suggested that the thermosphere hosted
291 much more water during the GDS than during the rest of the year. However, we note that the
292 only time when Stone et al. (2020) reported measurements around perihelion concerned the L_s
293 interval between 240° and 265° of MY33 (Figure 4 of Stone et al., 2020). It showed the same
294 rough trend as during the onset of the MY34 GDS, with values far exceeding those reported for
295 the regional dust storm of MY33, still a factor of 3 smaller than during the GDS.

296 Our results remain in line with the conclusion of Fedorova et al. (2020, 2021) that the
297 perihelion season is the primary conveyor of water to high altitudes on a long-term basis. The
298 high values above 100 km fill the gap between the water observed below 100 km and water ions
299 measured by NGIMS at 150 km. Both measurements bring unique constraints in our attempt to
300 understand how the water in the lower atmosphere connects with the escaping hydrogen in the
301 exosphere, an essential step before confidently extrapolating the water escape back in time.

302 Acknowledgments, Samples, and Data

303 ExoMars is a joint space mission of the European Space Agency (ESA) and Roscosmos.
304 The ACS experiment is led by the Space Research Institute (IKI) in Moscow, assisted by
305 LATMOS in France. Retrievals and analysis of temperature and water distributions in IKI are
306 funded by grant #20-42-09035 of the Russian Science Foundation. The ACS MIR data are
307 available from ESA's Planetary Science Archive at
308 <https://archives.esac.esa.int/psa/#!Table%20View/ACS=instrument>. The retrieved data with
309 altitude profiles of H₂O VMR for the considered seasons are available at
310 [https://data.mendeley.com/datasets/995y7ymdgm/draft?a=daa72362-898d-4c86-8a13-
311 023b4b59134c](https://data.mendeley.com/datasets/995y7ymdgm/draft?a=daa72362-898d-4c86-8a13-023b4b59134c).

312 References

313 Alday, J., Wilson C. F., Irwin, P. G. J., Olsen, K. S., Baggio, L., Montmessin, F., et al. (2019).
314 Oxygen isotopic ratios in Martian water vapour observed by ACS MIR on board the
315 ExoMars Trace Gas Orbiter. *Astronomy and Astrophysics*, 630, A91. doi:10.1051/0004-
316 6361/201936234.

- 317 Alday, J., Trokhimovskiy, A., Irwin, P. G. J., Wilson, C. F., Montmessin, F., Lefèvre, F., et al.
318 (2021). Isotopic fractionation of water and its photolytic products in the atmosphere of
319 Mars. *Nature Astronomy* (revised version NATASTRON-20123971B).
- 320 Aoki, S., Vandaele, A. C., Daerden, F., Villanueva, G. L., Liuzzi, G., Thomas, I. R., et al. (2019).
321 Water Vapor Vertical Profiles on Mars in Dust Storms Observed by TGO/NOMAD.
322 *Journal of Geophysical Research: Planets*, 124(12), 3482-3497.
323 doi:10.1029/2019je006109.
- 324 Belyaev, D. (2021). Revealing a High Water Abundance in the Upper Mesosphere of Mars with
325 ACS onboard TGO. *Mendeley Data*, v1. <http://dx.doi.org/10.17632/995y7ymdgm.1>
- 326 Benna, M., Mahaffy, P. R., Grebowsky, J. M., Fox, J. L., Yelle, R. V., & Jakosky, B. M. (2015).
327 First measurements of composition and dynamics of the Martian ionosphere by
328 MAVEN's Neutral Gas and Ion Mass Spectrometer. *Geophysical Research Letters*, 42,
329 8958–8965, doi:10.1002/2015GL066146.
- 330 Chaffin, M., Deighan, J., Schneider, N., & Stewart, A. (2017). Elevated atmospheric escape of
331 atomic hydrogen from Mars induced by high-altitude water. *Nature Geoscience*, 10(3),
332 174. doi:10.1038/ngeo2887.
- 333 Clancy, R. T., Grossman, A. W., Wolff, M. J., James, P. B., Rudy, D. J., Billawala, Y. N., et al.
334 (1996). Water vapor saturation at low altitudes around Mars aphelion: A key to Mars
335 climate? *Icarus*, 122(1), 36-62. doi:10.1006/icar.1996.0108.
- 336 Clancy, R. T., Smith, M. D., Lefèvre, F., McConnochie, T. H., Sandor, B. J., et al. (2017).
337 Vertical profiles of Mars 1.27 μm O₂ dayglow from MRO CRISM limb spectra:
338 Seasonal/global behaviors, comparisons to LMDGCM simulations, and a global
339 definition for Mars water vapor profiles. *Icarus*, 293, 132-156.
340 doi:10.1016/j.icarus.2017.04.011
- 341 Fedorova, A., Bertaux, J.-L., Betsis, D., Montmessin, F., Korablev, O., Maltagliati, L., & Clarke,
342 J. (2018). Water vapor in the middle atmosphere of Mars during the 2007 global dust
343 storm. *Icarus*, 300, 440–457.
- 344 Fedorova, A. A., Montmessin, F., Korablev, O., Luginin, M., Trokhimovskiy, A., Belyaev, D.
345 A., et al. (2020). Stormy water on Mars: The distribution and saturation of atmospheric
346 water during the dusty season. *Science*, 367(6475), 297-300.
347 doi:10.1126/science.aay9522.
- 348 Fedorova, A., Montmessin, F., Korablev, O., Lefèvre, F., Trokhimovskiy, A., & Bertaux, J. L.
349 (2021). Multi-annual monitoring of the water vapor vertical distribution on Mars by
350 SPICAM on Mars Express. *Journal of Geophysical Research: Planets*, 126,
351 e2020JE006616. doi:10.1029/2020JE006616.
- 352 Fox, J. L., Benna, M., Mahaffy, P. R., & Jakosky B. M. (2015). Water and water ions in the
353 Martian thermosphere/ionosphere. *Geophysical Research Letters*, 42, 8977–8985,
354 doi:10.1002/2015GL065465.
- 355 Gamache, R. R., Faresse, M., & Renaud, C. L. (2016). A spectral line list for water isotopologues
356 in the 1100–4100 cm⁻¹ region for application to CO₂-rich planetary atmospheres. *Journal*
357 *of Molecular Spectroscopy*, 326, 144-150. doi:10.1016/j.jms.2015.09.001.

- 358 Gordon, I. E., Rothman, L. S., Hill, C., Kochanov, R. V., Tan, Y., Bernath, P. F., et al. (2017).
359 The HITRAN2016 molecular spectroscopic database. *Journal of Quantum Spectroscopy*
360 *and Radiative Transfer*, 203, 3–69. doi:10.1016/j.jqsrt.2017.06.038.
- 361 Heavens, N. G., Kleinböhl, A., Chaffin, M. S., Halekas, J. S., Kass, D. M., Hayne, P. O., et al.
362 (2018). Hydrogen escape from Mars enhanced by deep convection in dust storms. *Nature*
363 *Astronomy*, 2(2), 126-132. doi:10.1038/s41550-017-0353-4.
- 364 Heavens, N. G., Kass, D. M., & Shirley, J. H. (2019). Dusty deep convection in the mars year 34
365 planet-encircling dust event. *Journal of Geophysical Research: Planets*, 124(11), 2863–
366 2892. <https://doi.org/10.1029/2019JE006110>.
- 367 Jakosky, B. M. (1985). The seasonal cycle of water on Mars. *Space Science Review*, 41, 131–
368 200. doi:10.1007/BF00241348.
- 369 Korablev, O. I., Montmessin, F., Trokhimovskiy, A., Fedorova, A. A., Shakun, A. V., Grigoriev,
370 A. V., et al. (2018). The Atmospheric Chemistry Suite (ACS) of Three Spectrometers for
371 the ExoMars 2016 Trace Gas Orbiter. *Space Science Review*, 214(1).
372 doi:10.1007/s11214-017-0437-6
- 373 Krasnopolsky, V. A. (2002). Mars' upper atmosphere and ionosphere at low, medium, and high
374 solar activities: implications for evolution of water. *Journal of Geophysical Research*,
375 107(E12), 5128. doi:10.1029/2001JE001809.
- 376 Krasnopolsky, V. A. (2015). Variations of the HDO/H₂O ratio in the martian atmosphere and
377 loss of water from Mars. *Icarus*, 257, 377–386. doi:10.1016/j.icarus.2015.05.021.
- 378 Krasnopolsky, V. A. (2019). Photochemistry of water in the martian thermosphere and its effect
379 on hydrogen escape. *Icarus*, 321, 62–70. doi:10.1016/j.icarus.2018.10.033.
- 380 Malathy Devi, V., Benner, D. C., Sung, K., Crawford, T. J., Gamache, R. R., Renaud, C. L., et
381 al. (2017). Line parameters for CO₂- and self-broadening in the ν₃ band of HD¹⁶O.
382 *Journal of Quantum Spectroscopy and Radiative Transfer*, 203, 158–174.
383 doi:10.1016/j.jqsrt.2017.02.020.
- 384 Maltagliati, L., Montmessin, F., Korablev, O., Fedorova, A., Forget, F., Määttänen, A., Lefèvre,
385 F., & Bertaux, J.-L. (2013). Annual survey of water vapor vertical distribution and water–
386 aerosol coupling in the martian atmosphere observed by SPICAM/MEx solar
387 occultations. *Icarus*, 223, 942–962. doi:10.1016/j.icarus.2012.12.012.
- 388 Marquardt, D. (1963). An Algorithm for Least-Squares Estimation of Nonlinear Parameters".
389 SIAM. *Journal on Applied Mathematics*, 11(2), 431–441. doi:10.1137/0111030.
- 390 Millour, E., Forget, F., Spiga, A., Vals, M., Zakharov, V., Montabone, L., et al. (2018). *The Mars*
391 *Climate Database (version 5.3)*. Paper presented at the Mars Science Workshop "From
392 Mars Express to ExoMars", held 27-28 February 2018 at ESAC, Madrid, Spain, id.68.
393 <https://www.cosmos.esa.int/web/mars-science-workshop-2018>.
- 394 McElroy, M. B., & Donahue, T. M. (1972). Stability of the Martian atmosphere. *Science*,
395 177(4053), 986-8 986. doi:10.1126/science.177.4053.986.
- 396 Montabone, L., Spiga, A., Kass, D. M., Kleinböhl, A., Forget, F., & Millour, E. (2020). Martian
397 Year 34 column dust climatology from Mars Climate Sounder observations:

- 398 Reconstructed maps and model simulations. *Journal of Geophysical Research: Planets*,
399 125(8), e061111. doi:10.1029/2019JE006111.
- 400 Montmessin, F., Fouchet, T., & Forget, F. (2005). Modeling the annual cycle of HDO in the
401 Martian atmosphere. *Journal of Geophysical Research: Planets*, 110, E03006.
402 doi:10.1029/2004JE002357
- 403 Neary, L., Daerden, F., Aoki, S., Whiteway, J., Clancy, R., Smith, M., et al. (2020). Explanation
404 for the increase in high-altitude water on Mars observed by NOMAD during the 2018
405 global dust storm. *Geophysical Research Letters*, 47(7), e2019GL084354.
406 <https://doi.org/10.1029/2019GL084354>.
- 407 Owen, T., Maillard, J. P., de Bergh, C., & Lutz, B. L. (1988). Deuterium on Mars: The
408 abundance of HDO and the value of D/H. *Science*, 240, 1767–1770.
409 doi:10.1126/science.240.4860.1767.
- 410 Richardson, M. I., & Wilson, R. J. (2002). Investigation of the nature and stability of the Martian
411 seasonal water cycle with a general circulation model. *Journal of Geophysical Research*,
412 107(E5), 5031, doi:10.1029/2001JE001536.
- 413 Rodin, A. V., Korablev, O. I., & Moroz, V. I. (1997). Vertical distribution of water in the near-
414 equatorial troposphere of Mars: water vapor and clouds. *Icarus*, 125(1), 212-229.
415 doi:10.1006/icar.1996.5602.
- 416 Rossi, L., Vals, M., Montmessin, F., Forget, F., Millour, E., Fedorova, A., Trokhimovskiy, A., &
417 Korablev, O., (2021). The Effect of the Martian 2018 Global Dust Storm on HDO as
418 Predicted by a Mars Global Climate Model. *Geophysical Research Letters*,
419 48(7), <https://doi.org/10.1029/2020GL090962>.
- 420 Shaposhnikov, D. S., Medvedev, A. S., Rodin, A. V., & Hartogh, P. (2019). Seasonal water
421 “pump” in the atmosphere of mars: Vertical transport to the thermosphere. *Geophysical*
422 *Research Letters*, 46, 4161–4169. doi:10.1029/2019GL082839.
- 423 Stone, W., Yelle, R. V., Benna, M., Lo, D. Y., Elrod, M. K., & Mahaffy P. R. (2020). Hydrogen
424 escape from Mars is driven by seasonal and dust storm transport of water. *Science*,
425 370(6518), 824–831. doi:10.1126/science.aba5229.
- 426 Villanueva, G. L., Liuzzi, G., Crismani, M. M. J., Aoki, S., Vandaele, A. C., et al. (2021). Water
427 heavily fractionated as it ascends on Mars as revealed by ExoMars/NOMAD. *Science*
428 *Advances*, 7(7), eabc8843. doi:10.1126/sciadv.abc8843.
- 429 Wang, H., & Richardson, M. I. (2015). The origin, evolution, and trajectory of large dust storms
430 on Mars during Mars years 24-30 (1999-2011). *Icarus*, 251, 112-127.
431 doi:10.1016/j.icarus.2013.10.033.
- 432 Zurek, R. W. & Martin, L. J. (1993). Interannual variability of planet-encircling dust storms on
433 Mars. *Journal of Geophysical Research*, 98(E2), 3247-3259. doi:10.1029/92JE02936.